CrossMark

Full paper

Alkalized Ti$_3$C$_2$ MXene nanoribbons with expanded interlayer spacing for high-capacity sodium and potassium ion batteries

Peichao Lian[a,1], Yanfeng Dong[a,1], Zhong-Shuai Wu[a,*], Shuanghao Zheng[a,b,d], Xiaohui Wang[c], Sen Wang[a,d], Chenglin Sun[a], Jieqiong Qin[a,d], Xiaoyu Shi[a,b,e], Xinhe Bao[a,b]

[a] Dalian National Laboratory for Clean Energy, Dalian Institute of Chemical Physics, Chinese Academy of Sciences, 457 Zhongshan Road, Dalian 116023, China
[b] State Key Laboratory of Catalysis, Dalian Institute of Chemical Physics, Chinese Academy of Sciences, 457 Zhongshan Road, Dalian 116023, China
[c] Shenyang National Laboratory for Materials Science, Institute of Metal Research, Chinese Academy of Sciences, 72 Wenhua Road, Shenyang 110016, China
[d] University of Chinese Academy of Sciences, 19A Yuquan Road, Shijingshan District, Beijing 100049, China
[e] Department of Chemical Physics, University of Science and Technology of China, 96 JinZhai Road, Hefei 230026, China

ARTICLE INFO

ABSTRACT

As post-lithium ion batteries, both sodium ion batteries (SIBs) and potassium ion batteries (PIBs) possess great potential for large scale energy storage. However, the improvements of both SIBs and PIBs for practical applications are facing great challenges in the development of high-performance electrode materials. Here, we demonstrate the fabrication of alkalized Ti$_3$C$_2$ (a-Ti$_3$C$_2$) MXene nanoribbons attained by continuous shaking treatment of pristine Ti$_3$C$_2$ MXene in aqueous KOH solution. Benefited from the expanded interlayer spacing of a-Ti$_3$C$_2$, narrow widths of nanoribbons as well as three-dimensional interconnected porous frameworks for enhanced ion reaction kinetics and improved structure stability, the resulting a-Ti$_3$C$_2$ anodes showed excellent sodium/potassium storage performance, for example, high reversible capacities of 168 and 136 mA h g^{-1} at 20 mA g^{-1} and 84 and 78 mA h g^{-1} at 200 mA g^{-1} were obtained for SIBs and PIBs, respectively. Notably, a-Ti$_3$C$_2$ possessed outstanding long-term cyclability at high current density of 200 mA g^{-1}, delivering a capacity of ∼ 50 mA h g^{-1} for SIBs and ∼ 42 mA h g^{-1} for PIBs after 500 cycles, which outperformed most of reported MXene based anodes for SIBs and PIBs. Moreover, this alkalization strategy could be extended as a universal approach for fabricating various alkalized MXene-based frameworks derived from a large family of MAX phases for numerous applications, such as catalysis, energy storage and conversion.

1. Introduction

With growing global concerns of increased energy and environmental issues, electrochemical energy storage technologies, possessing high round-trip efficiency, flexible power, long span life, and low maintenance, have received considerable attention for portable electronic devices, electric/hybrid electric vehicles (EV/HEV), large-scale power grid and microgrid systems [1–3]. Among them, lithium ion batteries (LIBs) are the major energy storage system for primary portable electronics and EV/HEV [4–6]. However, the ever-increasing demand of LIBs is greatly hampered by limited available lithium resources, rising cost, and safety issue. To overcome these shortcomings of LIBs, rechargeable sodium ion batteries (SIBs) are regarded as a potential competitive alternative because of their rich abundance, low cost, high energy density approaching to LIBs, and suitable redox potential ($E^o_{Na+/Na}$ = 2.71 V versus standard hydrogen electrode) [7–10].

Apart from SIBs, other non-lithium ion batteries, e.g., K-ion [11–13], Al-ion [14–16], Mg-ion [17,18], Ca-ion [19,20], also hold promise for next-generation energy storage systems. Unfortunately, the improvements of these non-lithium ion batteries for actual applications are facing great challenges in both optimum electrolytes and electrode materials [21,22]. For instance, graphite is a commercially available anode for LIBs, but incapable for SIBs due to the insufficient interlayer spacing [23]. Therefore, further development of high-performance electrode materials for non-lithium (Na$^+$, K$^+$) ion batteries is a pressing task.

Recently, MXenes, a large family of 2D transition metal carbides and carbonitrides [24–28], discovered by Gogotsi's group, have gained widespread interest as emerging potential host materials for metal (Li [29,30], Na [31–33], K [31], Mg [34]) ion batteries due to their unique morphology, high theoretical capacity (447.8, 351.8, 191.8 mA h g^{-1} for Li, Na, K on Ti$_3$C$_2$, respectively) [35], and flexible interlayer space capable of handling high rate capability [36]. In general, MXene was

fabricated by selective extraction of A layer from ternary metal carbides $M_{n+1}AX_n$ (where M = Ti, V, Nb, Ta, Zr, etc.; A = Al, Si, etc.; X = C, N; n = 1–3) with concentrated hydrofluoric acid or a mixed solution of lithium fluoride and hydrochloric acid [37]. Using these strategies, a large number of MXenes have been synthesized, e.g., Ti_3C_2 [24], Ti_2C [33], Ta_4C_3 [38], Mo_2C [39,40], V_2C [41], Nb_2C [41], Ti_3CN [38], Nb_4C_3 [42], $(Ti_{0.5}Nb_{0.5})_2C$ [38], $(V_{0.5}Cr_{0.5})_3C_2$ [38], and substantially accelerated their energy storage uses in batteries and supercapacitors [43–47]. It is reported that Ti_3C_2 MXene nanosheets (MNSs) for LIBs delivered a capacity of 320–410 mA h g^{-1}, and better rate capability than graphite due to the unconventional Li multilayer adsorption and small diffusion barrier of Li atoms on Ti_3C_2 [24,25]. Furthermore, Ti_3C_2 MNSs exhibited great promise for supercapacitors, with remarkable volumetric capacitance of 300–900 F cm^{-3}, in which a variety of cations, e.g., Li$^+$, Na$^+$, K$^+$, Mg^{2+}, Al^{3+}, can be intercalated electrochemically for charge storage [48,49]. More recently, theoretical simulations and experimental measurements revealed that MNSs would be a suitable host material for sodium and potassium storage with excellent rate capability and long cycling life [31–33,35,50]. Of vital significance is that the pillaring effect of trapped Na$^+$ disclosed can greatly stabilize the constant interlayer distance for fast reversible sodiation and desodiation [32]. Despite of significant advances on MNSs, rational synthesis of novel MXene based nanoarchitectures, e.g., nanoribbons, for energy storage is highly elusive.

Here we report, for the first time, the fabrication of three-dimensional (3D) porous frameworks of alkalized Ti_3C_2 (a-Ti_3C_2) MXene nanoribbons (MNRs), with expanded interlayer spacing, as anode materials for stable SIBs and potassium ion batteries (PIBs) with outstanding capacities, excellent rate capability and long-term cyclability. The a-Ti_3C_2 MNRs were prepared from the HF-etched, organ-like Ti_3C_2 MNSs by continuous shaking treatment in aqueous KOH solution for 72 h, in which the alkalization and delamination were simultaneously implemented. The as-prepared a-Ti_3C_2 exhibited an expanded interlayer d-spacing of 12.5 Å, oxygen-terminated surface, narrow widths of 6–22 nm, and 3D porous interconnected framework, which are favorable for increased ion storage and fast ion diffusion along the interlamination nanochannels, and rapid electron transport throughout 3D porous structure. As a result, such a-Ti_3C_2 MNRs showed great promise as anodes for SIBs and PIBs with remarkable capacities and excellent rate capability. High reversible capacities of 168 and 136 mA h g^{-1} at 20 mA g^{-1} and 84 and 78 mA h g^{-1} at 200 mA g^{-1} were obtained for SIBs and PIBs, respectively. Notably, a-Ti_3C_2 MNRs possessed outstanding long-term cyclability at high current density of 200 mA g^{-1}, delivering a capacity of ~ 50 mA h g^{-1} for SIBs and ~ 42 mA h g^{-1} for PIBs after 500 cycles. Moreover, this approach is flexible and scalable, and can be as a general strategy for fabricating many alkalized MXene-based materials, derived from 60 + group of MAX phases [37], for numerous excited applications such as supercapacitors, batteries, and electrocatalysis.

2. Experimental

2.1. Materials preparation

The Ti_3AlC_2 powder was prepared by a solid-liquid reaction method [51,52]. Typically, the powders of Ti (99%, 300 mesh), Al (99%, 10 μm) and graphite (99%, 6.5 μm) in a molar ratio of 3:1.1:1.88 were mixed for 12 h with agate balls and absolute alcohol in an agate jar, followed by drying at 70 °C for 8 h in air. The resulting mixture was uniaxially cold pressed into a green compact in a graphite mould. Subsequently, the compact together with the mould was heated in a furnace at 1550 °C for 2 h in a flowing Ar atmosphere. Finally, the sample was naturally cooled down to room temperature.

To prepare a-Ti_3C_2 MNRs, first, Ti_3C_2 MNSs were synthesized in a sealed plastic container by shaking treatment of the pristine MAX phase of Ti_3AlC_2 (0.5 g) in 60 mL aqueous HF solution (40%) for 72 h with

programmable incubator shaker (SHIPING Temperature SPH-100F), and collected by high-speed centrifugation at 6500 rpm for 5 min. After centrifugation and washing with deionized water three times, the HF-etched powder was dried in vacuum at 60 °C for 12 h. Subsequently, the a-Ti_3C_2 MNRs were prepared by continuous shaking treatment (250 rpm) of Ti_3C_2 MNRs (1.0 g) at room temperature (25 °C) in 120 mL 6 M KOH aqueous solution for 72 h in a sealed container with Ar atmosphere, and harvested after rinsing and vacuum drying at 60 °C for 24 h.

2.2. Material characterization

Materials characterization was conducted by scanning electron microscope (SEM, JEOL JSM-7800F), transmission electron microscope (TEM, JEM-2100), scanning transmission electron microscopy (STEM, FEI Tecnai G^2 F20), X-ray diffraction (XRD) patterns (X'pert Pro), X-ray photoelectron spectroscopy (XPS, Thermo ESCALAB 250Xi equipped with monochromatic Al Kα source of 1486.5 eV), Fourier transform infrared (FT-IR) spectoscopy (Bruker, Hyperion 3000), nitrogen sorption isotherm plots (a Quadrasorb SI analyzer).

2.3. Electrochemical measurement

Both the tests of SIBs and PIBs were conducted using CR2016 coin cells with sodium or potassium foil as the counter and reference electrodes. The galvanostatic charge/discharge tests were performed using a LAND CT2001A battery system. Cyclic voltammetry studies were carried out on a CHI 760E electrochemical workstation at a scan rate of 0.1 mV s^{-1} between 0.01 and 3 V. The working electrodes (12 mm in diameter) consist of active material (a-Ti_3C_2 MNRs, Ti_3C_2 MNSs), carbon black, and polyvinylidene fluoride in a weight ratio of 7:2:1. The electrolyte used was 1.0 M NaCF$_3$SO$_3$ in diglyme electrolyte for SIBs, and 0.8 M KPF$_6$ in EC/DEC (1: 1, v/v) electrolyte for PIBs, tested between 0.01 and 3.0 V.

3. Results and discussion

A schematic for synthesizing a-Ti_3C_2 MNRs was illustrated in Fig. 1a. First, Ti_3AlC_2 was synthesized by solid-liquid reaction of ball-milled Ti, Al and graphite powder in a molar ratio of 3:1.1:1.88 at 1550 °C for 2 h under an argon flow [51,52]. SEM images of the Ti_3AlC_2 powder showed a densely layer-stacked structure with micrometer size distribution (Fig. 1b and Fig. S1). Second, the resulting Ti_3AlC_2 was exfoliated into few-nanometer-thick multilayer MNSs (Ti_3C_2) by extraction of the Al layer in concentrated HF solution [24]. A loosely layered organ-like structure was observed from Ti_3C_2 MNSs, indicative of the successful exfoliation (Fig. 1c, Fig. S2a) [38]. High-magnification SEM images of the interconnected multilayers disclosed a thickness of 20–50 nm (Fig. S2b), consisting of exfoliated individual monolayers [25]. Third, the HF-etched Ti_3C_2 MNSs were treated in alkaline KOH solution by continuous shaking. In this process, alkalization promoted further expansion of interlayer spacing, thus resulting in their delamination of Ti_3C_2 MNSs into MNRs. With the extended time up to 72 h, a 3D porous framework of alkalized MNRs was obtained (Fig. 1d).

The morphology of a-Ti_3C_2 MNRs was examined by SEM and TEM (Fig. 2, Fig. S3). Low-magnification SEM images showed the size of MNR macroscale aggregates ranging from several to twenty micrometers (Fig. 1d), and 3D interconnected porous framework (Fig. 2a, Fig. S3a), while high-magnification SEM (Fig. 2c, Fig. S3b) and TEM (Fig. 2c, Fig. S3c) images of 3D porous framework clearly displayed the interconnected microstructure of elongated MNRs. High-resolution TEM (HRTEM) images (Fig. 2d-f, and Fig. S3d) unraveled good phase crystallinity and narrow width distribution, e.g., around 6–22 nm, of a-Ti_3C_2 MNRs. It is noteworthy that three typical microstructures of MNRs, e.g., flat nanoribbon (Fig. 2d, f), self-twisted nanoribbon (Fig. 2e), and two jointed nanoribbons (Fig. S3d), were observed in the
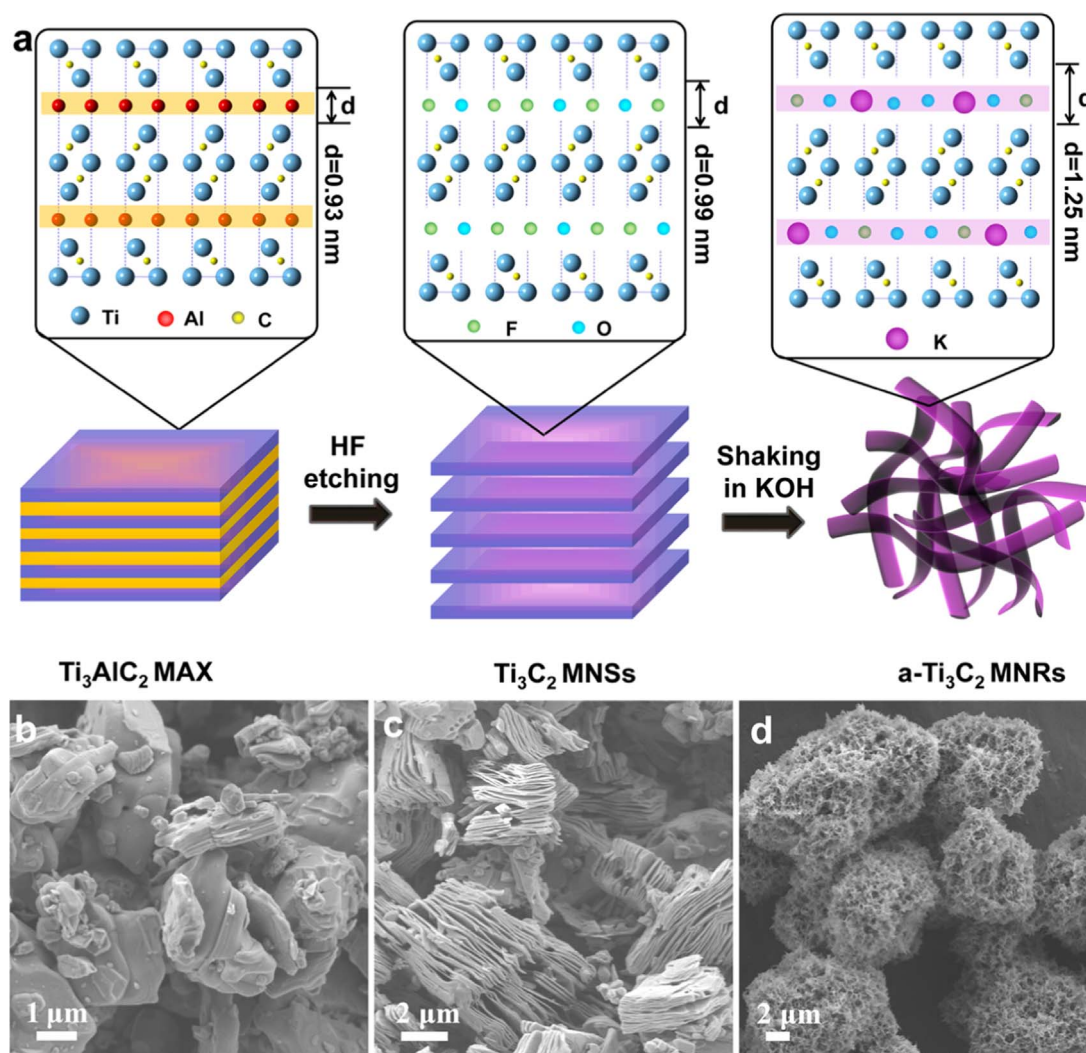
Fig. 1. Fabrication of a-Ti$_3$C$_2$ MNRs. (a) Schematic of synthesis of a-Ti$_3$C$_2$ MNRs. First, the synthesis of Ti$_3$AlC$_2$ MAX phase. Second, the Al layer is extracted from the corresponding MAX phase with 40% HF aqueous solution to obtain Ti$_3$C$_2$ MNSs. Third, the Ti$_3$C$_2$ MNSs are treated with KOH solution under continuous shaking condition, producing a-Ti$_3$C$_2$ MNRs. (b-d) Low-magnification SEM images of the corresponding (b) Ti$_3$AlC$_2$, (c) Ti$_3$C$_2$ MNSs, and (d) a-Ti$_3$C$_2$ MNRs, respectively.

framework. In addition, energy dispersive X-ray (EDX) elemental mapping analysis demonstrated the existence of C, K, O and F in a-Ti$_3$C$_2$ MNRs (Fig. 2g-k, Fig. S4), and the atomic ratio of Ti:C is 2.98:2, which is very close to the ideal ratio of Ti:C (3:2) in Ti$_3$C$_2$ MXene (Fig. S5).

The structural changes of a-Ti$_3$C$_2$ MNRs, Ti$_3$C$_2$ MNSs, and pristine Ti$_3$AlC$_2$ were investigated by their XRD patterns. As shown in Fig. 3a, XRD pattern validated the successful fabrication of pure Ti$_3$AlC$_2$ phase, which is in accordance with the standard spectrum (JCPDS 52-0875) [52]. After HF etching, the strongest XRD peak e.g., (104), in the out-of-plane direction was significantly weakened, and a broader peak of (002) corresponding to in-plane diffraction appeared at 2θ angel of 8.9° in Ti$_3$C$_2$, indicating the substantial expansion of the interlayer spacing from 9.3 Å for Ti$_3$AlC$_2$ to 9.9 Å for Ti$_3$C$_2$ [24]. When the HF-treated Ti$_3$C$_2$ MNSs were treated in KOH solution by continuous shaking, the (002) peak was shifted to 7.1°, with an increased d-spacing of 12.5 Å, demonstrative of the expansion of interlayer spacing. Notably, Ar atmosphere protection during shaking treating is necessary to avoid undesirable oxidization of Ti$_3$C$_2$ (Fig. S6). Furthermore, HRTEM image clearly clarified the layered nanostructure of a-Ti$_3$C$_2$, without observable crystalline TiO$_2$ (Fig. S7).

XPS was further applied to probe the composition evolution of a-Ti$_3$C$_2$ MNRs, Ti$_3$C$_2$ MNSs, and Ti$_3$AlC$_2$. Both the C1s XPS (Fig. 3b) and Ti2p XPS (Fig. S8) spectra showed the characteristic peaks of Ti–C and Ti–O bonds, which is in good agreement with the previous literature

[24]. Remarkably, the characteristic peaks of K2p$_{3/2}$ at 292.4 eV and K2p$_{1/2}$ at 295.2 eV were displayed only from a-Ti$_3$C$_2$ MNRs, but no potassium signal was detected in both Ti$_3$C$_2$ and Ti$_3$AlC$_2$ (Fig. 3b). This accounts for the alkalization of MNRs, consistent with XRD measurement. Moreover, in comparison with Ti$_3$C$_2$ and Ti$_3$AlC$_2$, the O1s XPS in a-Ti$_3$C$_2$ MNRs appeared a distinguishable signal with respect to the Ti-O group at 529.6 eV (Fig. 3c), suggestive of increased concentration of OH groups [25,53]. Meanwhile, the F1s XPS spectrum of a-Ti$_3$C$_2$ MNRs was almost unobservable (Fig. S8a), demonstrating the essential substitution of F atoms with OH groups after alkalization, and consequently the formation of O-terminated Ti$_3$C$_2$ MNRs [30,53]. This result was also affirmed by FT-IR spectrum of a-Ti$_3$C$_2$ MNRs with the strong OH peaks at 3415 and 1624 cm^{-1}, both of which, however, are nearly absent in Ti$_3$C$_2$ and Ti$_3$AlC$_2$ (Fig. S9) [30]. In addition, nitrogen sorption analysis of a-Ti$_3$C$_2$ MNRs exhibited a specific surface area of ~ 25.0 m^2 g^{-1}, which is higher than those of Ti$_3$C$_2$ MNSs (~ 4.0 m^2 g^{-1}) and Ti$_3$AlC$_2$ (~ 2.0 m^2 g^{-1}) (Fig. 3d). The increase in specific surface area for a-Ti$_3$C$_2$ was attributed to the nanoribbon structures of MNRs as well as 3D woven-like frameworks with open macropores.

Based on the above observations, we propose a possible formation mechanism of 3D porous framework of a-Ti$_3$C$_2$ MNRs as follows (Fig. S10a-d). Initially, the alkalization process of HF-etched Ti$_3$C$_2$ MNSs with KOH promoted the transformation from the F groups to OH groups on the surface and interlayer (Fig. S10a) [30], as confirmed by the XPS
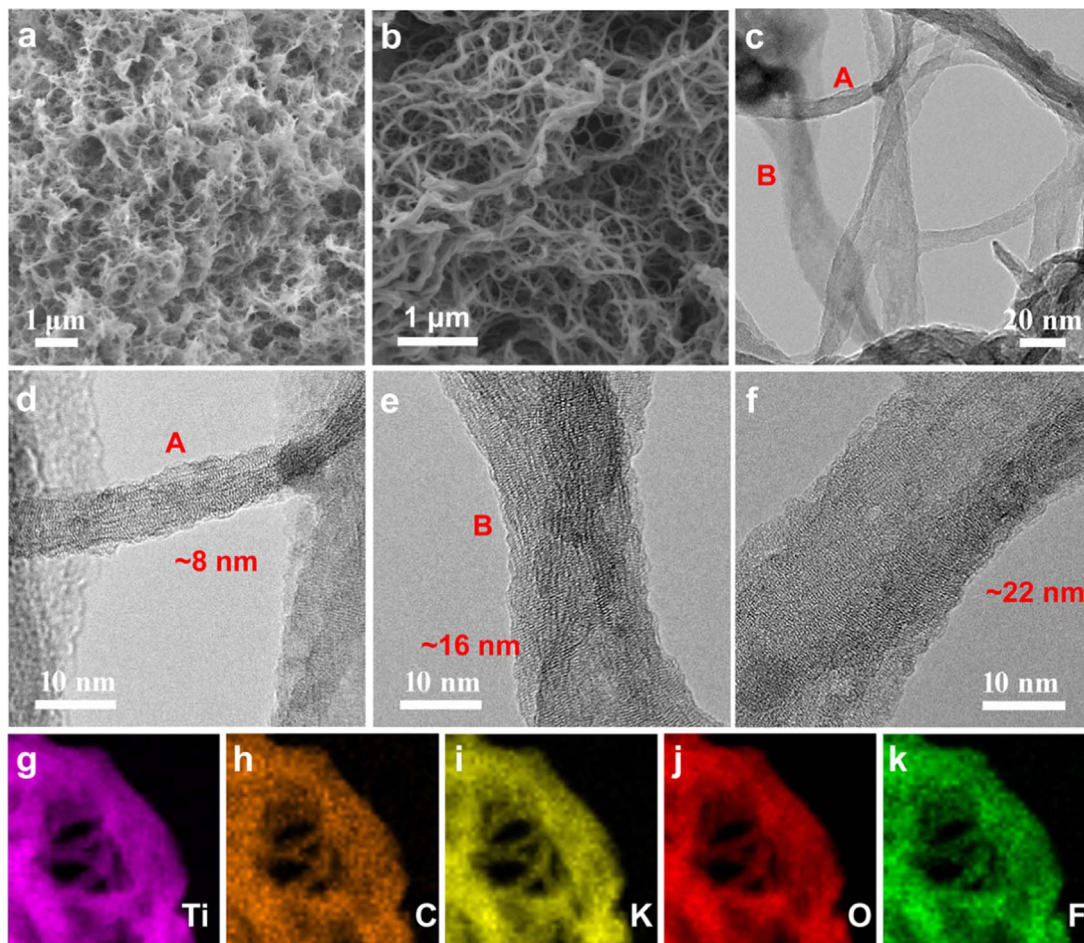
Fig. 2. Morphological characterization of a-Ti$_3$C$_2$ MNRs. (a) low-magnification and (b) high-magnification SEM images of a-Ti$_3$C$_2$ MNRs. (c) TEM images of a-Ti$_3$C$_2$ MNRs. (d-f) HRTEM images of a-Ti$_3$C$_2$ MNRs: (d) a single MNR with a width of ~ 8 nm, taken from the A position in (c), (e) a self-twisted MNR with ~ 16 nm, taken from the B position in (c), and (f) a flat MNR with a width of ~ 22 nm. (g-k) EDX elemental mapping images of (g) Ti, (h) C, (i) K, (j) O and (k) F in a-Ti$_3$C$_2$ MNRs.
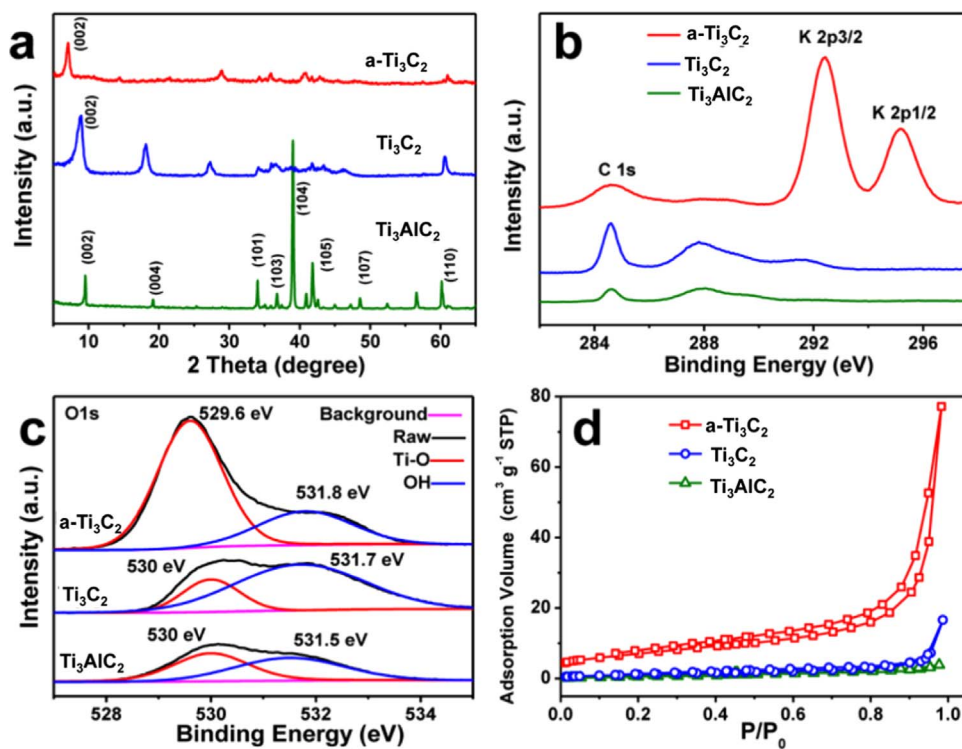

Fig. 3. Structural characterization of a-Ti$_3$C$_2$ MNRs, Ti$_3$C$_2$ MNSs, and pristine Ti$_3$AlC$_2$. (a) XRD patterns of a-Ti$_3$C$_2$, Ti$_3$C$_2$ and Ti$_3$AlC$_2$. (b) C1s XPS and K2p XPS and (c) O1s XPS spectra of a-Ti$_3$C$_2$, Ti$_3$C$_2$ and Ti$_3$AlC$_2$. (d) Nitrogen sorption isotherm plots of a-Ti$_3$C$_2$, Ti$_3$C$_2$ and Ti$_3$AlC$_2$.

(Fig. 3c) and FI-IR (Fig. S9) measurements. Subsequently, because of electrostatic interaction and ion exchange, this substitution of F groups with OH groups could strengthen rapid adsorption of K ions and intercalation of K^+ into multilayer MNSs, resulting in the substantial expansion of interlayer distance, which was validated by the XRD (Fig. 3a) and K2p XPS (Fig. 3b) results. Accordingly, the continuous shaking further enhanced the diffusion of K^+ and OH^- ions along the channels of interlamination (Fig. S10e), resulting in the gradual delamination of O-terminated a-Ti$_3$C$_2$ MNRs, and thus, splitting the short MNRs from the delaminated nanosheets. Notably, alkalization occurred as fast as 1 h (Fig. S11), while SEM images showed the generation of ultrasmall MNRs split from the stacked MNSs as fast as 1 h (Fig. S10b, f), and the appearance of longer MNRs at 3 and 6 h (Fig. S10c, g, h), respectively. With the extended time ($\geq$ 12 h), many longer MNRs were obtained (Fig. S10h, i). As a consequence, long MNRs were self-assembled to form 3D interconnected porous frameworks (Fig. S10d, i). It is emphasized that the shear force caused by shaking oriented to the flow direction of the fluid against MNSs played an important role in dominating the delamination and generation of the long elongated MNRs. Although more work is ongoing to understand the formation mechanism of MNRs, it is noteworthy that this novel MNR-based electrode with short ionic diffusion length, expanded interlayer space and 3D porous framework can be expected to offer efficient ion and electron transport pathways for achieving ultrafast rechargeable metal-ion batteries.

The electrochemical performance of the as-prepared a-Ti$_3$C$_2$ MNRs was examined for SIBs in 1 M NaCF$_3$SO$_3$ electrolyte and PIBs in 0.8 M KPF$_6$ electrolyte (Fig. 4). Fig. 4a shows cyclic voltammetry of a-Ti$_3$C$_2$ MNRs for SIBs measured at 0.1 mV s^{-1}. For comparison, Ti$_3$C$_2$ MNSs was also examined under the same conditions (Fig. S12). In the first cycle, two main cathodic peaks were observed at 1.50 V and 0.39 V (vs. Na$^+$/Na) for a-Ti$_3$C$_2$ MNRs, corresponding to Na$^+$ intercalation/sorption, and the formation of solid electrolyte interphase (SEI) film resulting from the electrolyte decomposition and irreversible reactions of Na$^+$ with water or unwashed etching products, respectively [31,32]. There were several sharp peaks around 0.01 V, which should be ascribed to some electrolyte deposition probably due to the low potential window of 0.01–3 V [54]. In the second cycle, the main intercalation peak was shifted to 1.1 V, and the peak intensity and integral areas were close to that of the third one for a-Ti$_3$C$_2$ MNRs (Fig. 4a). These results indicate that electrochemical reversibility was rapidly built after the initial three cycles. Interestingly, we observed that the reversible potential of Na$^+$ intercalation peak in the second cycle is $\sim$ 1.1 V, much

lower than that of the MNSs (2.1 V), which may be attributed to the expanded interlayer spacing [32].

Galvanostatic charge and discharge profiles of SIBs cycled at different current densities from 20 to 300 mA g^{-1} are presented in Fig. 4b and c. It can be seen that, after first sodiation and desodiation, a-Ti$_3$C$_2$ showed a discharge capacity of 304 mA h g^{-1} and charge capacity of 168 mA h g^{-1} at a current density of 20 mA g^{-1}, which are higher than those of stacked MNSs with 270 and 143 mA h g^{-1} at 20 mA g^{-1} [32], and comparable to the capacities of MXene/CNT film Ti$_2$CTx anode in a 1 M NaPF$_6$/EC-DEC electrolyte [33,50], and the discharge capacity is close to the theoretical value $\sim$ 351.8 mA h g^{-1} of Ti$_3$C$_2$ MNSs reported [35]. Fig. 4c showed the rate performance of a-Ti$_3$C$_2$ MNRs. It was disclosed that the reversible capacity varies from 167 (2nd cycle), 131 (12th cycle), 108 (22th cycle), 99 (32th cycle), 93 (42th cycle) to 85 mA h g^{-1} (52th cycle) with the increasing current density from 20, 50, 100, 150, 200 to 300 mA g^{-1} (Fig. 4b). These results greatly outperformed those of MNSs (Table S1), for instance, about 120, 101, 92, and 83 mA h g^{-1} at corresponding current densities of 20, 50, 100 and 200 mA g^{-1}, respectively [32]. Remarkably, the capacity then significantly increases back to 168 mA h g^{-1} after 60 cycles when the current density returned to 20 mA g^{-1}, maintaining about 100% of the initial reversible capacity at this rate (Fig. 4c). More importantly, a-Ti$_3$C$_2$ MNRs exhibited stable cycling performance, and delivered a high capacity of 113 mA h g^{-1} after 200 cycles at 50 mA g^{-1} (Fig. S13), indicating the robustness of structural integrity during repeatedly charge/discharge cycles. At higher current density of 200 mA g^{-1}, a-Ti$_3$C$_2$ nanoribbons also delivered stable cycling performance over 500 cycles (Fig. 4d), the slight capacitance loss at high current density is likely attributed to the rapid diffusion effect of Na$^+$ ions in the interlayer channels, causing the relative instability of structural integrity. The outstanding rate capability and long-term stability could result from large expanded interlayer space (12.5 Å) for both increased Na$^+$ storage and fast Na$^+$ diffusion along the interlamination nanochannels.

The electrochemical behavior of a-Ti$_3$C$_2$ MNRs was also investigated with respect to potassium storage as shown in Fig. 5. Similar to sodium storage, electrochemical reversibility was rapidly established in the initial three cycles, and a reversible K$^+$ intercalation peak was observed at $\sim$ 1.26 V (vs. K$^+$/K) in cyclic voltammetry (Fig. 5a). The capacity-voltage curves (Fig. 5b) showed the first discharge and charge capacities of 502 and 136 mA h g^{-1} at 20 mA g^{-1}, respectively. This discharge value is much higher than the theoretically predicted capacity of 191.8 mA h g^{-1} (single-site adsorption) [35] and the experimentally measured initial discharge value of 260 mA h g^{-1} for Ti$_3$C$_2$ (Table S2),
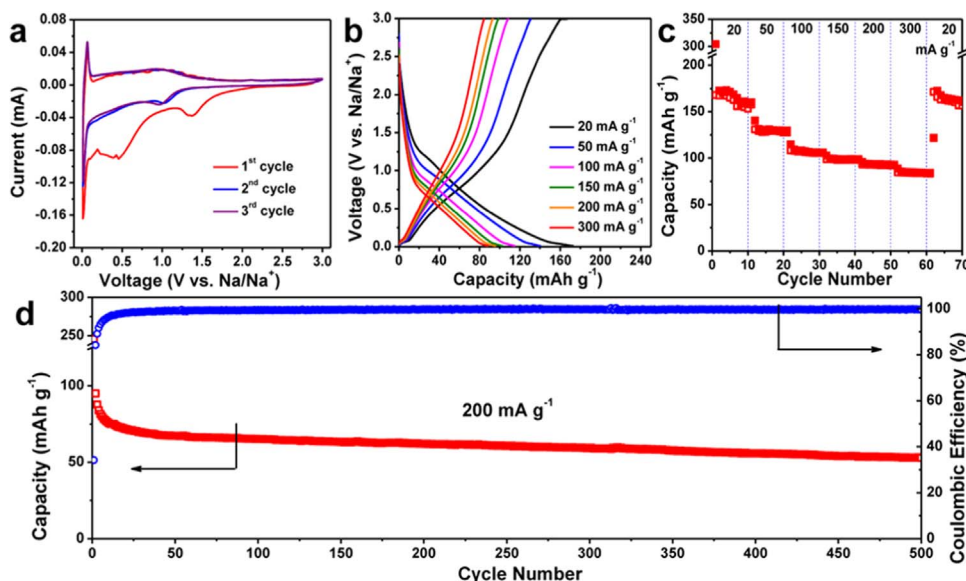

Fig. 4. Electrochemical characterizations of a-Ti$_3$C$_2$ MNRs for SIBs. (a) Cyclic voltammetry measured at 0.1 mV s^{-1} between 0.01 and 3 V, (b) Galvanostatic charge and discharge curves cycled at different current densities from 20 to 300 mA g^{-1}, and (c) rate performance of a-Ti$_3$C$_2$ MNRs. (d) Long-term cycling performance and Coulombic efficiency of a-Ti$_3$C$_2$ MNRs at a large current density of 200 mA g^{-1}.

Fig. 5. Electrochemical characterizations of a-Ti$_3$C$_2$ MNRs for PIBs. (a) Cyclic voltammetry measured at 0.1 mV s^{-1}, (b) Galvanostatic charge and discharge curves cycled at different current densities from 20 to 300 mA g^{-1}, and (c) rate performance of a-Ti$_3$C$_2$ MNRs. (d) Long-term cycling performance and Coulombic efficiency of a-Ti$_3$C$_2$ MNRs at a large current density of 200 mA g^{-1}.
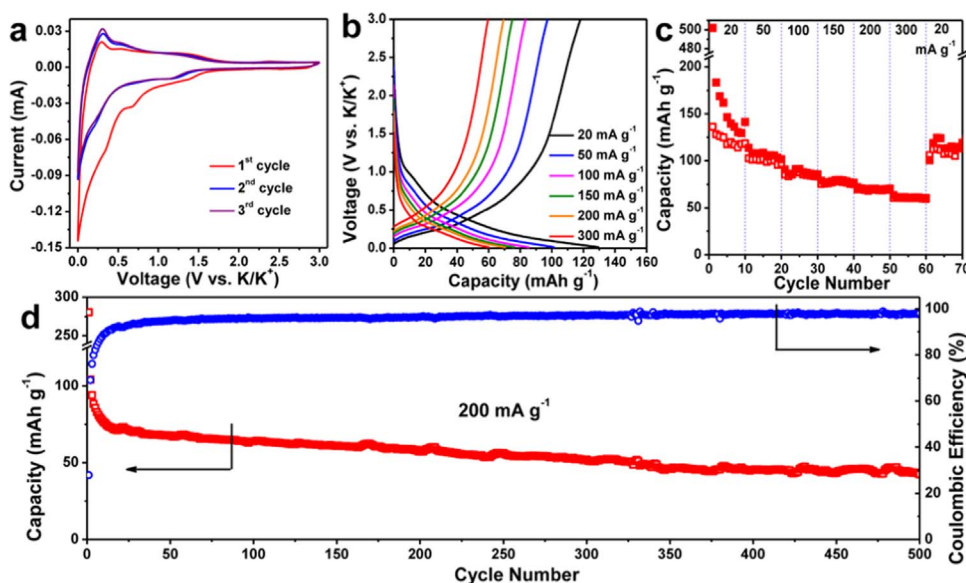
possibly due to the irreversible trapped K in SEI films and other adsorption of extra K ions [31]. Also, a-Ti$_3$C$_2$ MNRs displayed exceptional rate performance, achieving impressive charge capacities of 141 (10th cycle), 101 (20th cycle), 86 (30th cycle), 77 (40th cycle), 70 (50th cycle), and 60 (60th cycle) mA h g^{-1} at different current densities of 20, 50, 100, 150, 200, and 300 mA g^{-1}, respectively (Fig. 5c). Significantly, the capacity restored ~ 119 mA h g^{-1} after 60 cycles when the rate returned to 20 mA g^{-1} (Fig. 5c). Furthermore, the a-Ti$_3$C$_2$ MNRs for potassium storage also possessed long-term cyclability at a high current density of 200 mA g^{-1}, and maintained a reversible capacity of ~ 42 mA h g^{-1} after 500 cycles (Fig. 5d), which is slightly lower than that for sodium storage (~ 53 mA h g^{-1}). Certainly, this result can be explained by the larger radium of K$^+$ (1.40 Å [55]) than Na$^+$ (1.02 Å [56]). Nevertheless, the outstanding capacity, rate capability and long-term cyclability of a-Ti$_3$C$_2$ MNRs for both SIBs and PIBs are mainly attributed to expanded interlayer spacing, which is favorable for both increased charge storage and fast diffusion of Na$^+$/K$^+$ ions [31,32]. In addition, the unique 3D porous framework of a-Ti$_3$C$_2$ MNRs with reduced ion diffusion length, large specific surface area, high electronic conductivity, and oxygen-terminated surface [31] are also responsible for the overall enhancement for sodium and potassium storage.

4. Conclusion

In summary, we have demonstrated the fabrication of a novel 3D porous framework of alkalized Ti$_3$C$_2$ MNRs derived from Ti$_3$C$_2$ MNSs in KOH solution. This unique architecture synergistically combined nanoribbons with expanded interlayer spacing and 3D open porous network consisting of MNRs, enabling fast electron transport and rapid ion diffusion. These alkalized MNRs showed exceptional performance for SIBs and PIBs in term of remarkable capacity, excellent rate capability and outstanding cyclability. Moreover, this method for fabricating a-Ti$_3$C$_2$ MNRs is facile and scalable, and can be a general strategy for fabricating a large number of alkalized MXene materials since Ti$_3$C$_2$ is a member of a 60+ group of layered ternary carbides and nitrides [37]. In light of this, the performance of SIBs and PIBs can be further enhanced through (i) the design of other alkalized MXene (e.g., Nb$_2$CT$_x$ and Mo$_2$CT$_x$) nanoribbons with our developed alkalization strategy, (ii) synthesis of novel Ti-based nanostructures derived from a-Ti$_3$C$_2$ nanoribbons [57], and (iii) fabrication of a-Ti$_3$C$_2$ hybrids with other high-capacity electrochemical active materials [58]. Therefore, this finding will pave the way to synthesize a series of new MXene-based materials

for various applications such as supercapacitors [48,49], batteries [59], catalysts [60], thermal electricity [61], and sensors [62].

Appendix A. Supporting information

Supplementary data associated with this article can be found in the online version at http://dx.doi.org/10.1016/j.nanoen.2017.08.002.

References

[1] C. Liu, F. Li, L.P. Ma, H.M. Cheng, Adv. Mater. 22 (2010) E28–E62.
[2] J. Jiang, Y. Li, J. Liu, X. Huang, C. Yuan, X.W. Lou, Adv. Mater. 24 (2012) 5166–5180.
[3] P. Simon, Y. Gogotsi, B. Dunn, Science 343 (2014) 1210–1211.
[4] Y. Wang, G. Cao, Adv. Mater. 20 (2008) 2251–2269.
[5] Z.-S. Wu, G.M. Zhou, L.C. Yin, W.C. Ren, F. Li, H.M. Cheng, Nano Energy 1 (2012) 107–131.
[6] K.-X. Wang, X.-H. Li, J.-S. Chen, Adv. Mater. 27 (2015) 527–545.
[7] S.-W. Kim, D.-H. Seo, X. Ma, G. Ceder, K. Kang, Adv. Energy Mater. 2 (2012) 710–721.
[8] J. Yang, X. Zhou, D. Wu, X. Zhao, Z. Zhou, Adv. Mater. 29 (2017) 1604108.
[9] J. Xu, M. Wang, N.P. Wickramaratne, M. Jaroniec, S. Dou, L. Dai, Adv. Mater. 27 (2015) 2042–2048.
[10] N. Yabuuchi, K. Kubota, M. Dahbi, S. Komaba, Chem. Rev. 114 (2014) 11636–11682.
[11] D. Su, A. McDonagh, S.-Z. Qiao, G. Wang, Adv. Mater. 29 (2017) 1604007.
[12] Z.L. Jian, Z.Y. Xing, C. Bommier, Z.F. Li, X.L. Ji, Adv. Energy Mater. 6 (2016) 1501874.
[13] Z. Jian, W. Luo, X. Ji, J. Am. Chem. Soc. 137 (2015) 11566–11569.
[14] M.-C. Lin, M. Gong, B. Lu, Y. Wu, D.-Y. Wang, M. Guan, M. Angell, C. Chen, J. Yang, B.-J. Hwang, H. Dai, Nature 520 (2015) 324–328.
[15] X. Yu, B. Wang, D. Gong, Z. Xu, B. Lu, Adv. Mater. 29 (2017) 1604118.
[16] X. Tong, F. Zhang, B. Ji, M. Sheng, Y. Tang, Adv. Mater. 28 (2016) 9979–9985.
[17] B. Liu, T. Luo, G. Mu, X. Wang, D. Chen, G. Shen, ACS Nano 7 (2013) 8051–8058.
[18] S. Tepavcevic, Y. Liu, D. Zhou, B. Lai, J. Maser, X. Zuo, H. Chan, P. Král, C.S. Johnson, V. Stamenkovic, N.M. Markovic, T. Rajh, ACS Nano 9 (2015) 8194–8205.
[19] A.L. Lipson, B. Pan, S.H. Lapidus, C. Liao, J.T. Vaughey, B.J. Ingram, Chem. Mater.

    27 (2015) 8442–8447.

[20] D. Datta, J. Li, V.B. Shenoy, ACS Appl. Mater. Interfaces 6 (2014) 1788–1795.

[21] D. Kundu, E. Talaie, V. Duffort, L.F. Nazar, Angew. Chem. Int. Ed. 54 (2015) 3431–3448.

[22] M.D. Slater, D. Kim, E. Lee, C.S. Johnson, Adv. Funct. Mater. 23 (2013) 947–958.

[23] Y. Wen, K. He, Y. Zhu, F. Han, Y. Xu, I. Matsuda, Y. Ishii, J. Cumings, C. Wang, Nat. Commun. 5 (2014) 4033.

[24] M. Naguib, M. Kurtoglu, V. Presser, J. Lu, J.J. Niu, M. Heon, L. Hultman, Y. Gogotsi, M.W. Barsoum, Adv. Mater. 23 (2011) 4248–4253.

[25] O. Mashtalir, M. Naguib, V.N. Mochalin, Y. Dall'Agnese, M. Heon, M.W. Barsoum, Y. Gogotsi, Nat. Commun. 4 (2013) 1716.

[26] J.-C. Lei, X. Zhang, Z. Zhou, Front. Phys. 10 (2015) 276–286.

[27] B. Anasori, M.R. Lukatskaya, Y. Gogotsi, Nat. Rev. Mater. 2 (2017) 16098.

[28] Q. Tang, Z. Zhou, P. Shen, J. Am. Chem. Soc. 134 (2012) 16909–16916.

[29] M. Naguib, J. Come, B. Dyatkin, V. Presser, P.L. Taberna, P. Simon, M.W. Barsoum, Y. Gogotsi, Electrochem. Commun. 16 (2012) 61–64.

[30] J.M. Luo, X.Y. Tao, J. Zhang, Y. Xia, H. Huang, L.Y. Zhang, Y.P. Gan, C. Liang, W.K. Zhang, ACS Nano 10 (2016) 2491–2499.

[31] Y. Xie, Y. Dall'Agnese, M. Naguib, Y. Gogotsi, M.W. Barsoum, H.L.L. Zhuang, P.R.C. Kent, ACS Nano 8 (2014) 9606–9615.

[32] S. Kajiyama, L. Szabova, K. Sodeyama, H. Iinuma, R. Morita, K. Gotoh, Y. Tateyama, M. Okubo, A. Yamada, ACS Nano 10 (2016) 3334–3341.

[33] X. Wang, S. Kajiyama, H. Iinuma, E. Hosono, S. Oro, I. Moriguchi, M. Okubo, A. Yamada, Nat. Commun. 6 (2015) 6544.

[34] C. Eames, M.S. Islam, J. Am. Chem. Soc. 136 (2014) 16270–16276.

[35] D.Q. Er, J.W. Li, M. Naguib, Y. Gogotsi, V.B. Shenoy, ACS Appl. Mater. Interfaces 6 (2014) 11173–11179.

[36] X. Liang, A. Garsuch, L.F. Nazar, Angew. Chem. Int. Ed. 54 (2015) 3907–3911.

[37] M. Naguib, V.N. Mochalin, M.W. Barsoum, Y. Gogotsi, Adv. Mater. 26 (2014) 992–1005.

[38] M. Naguib, O. Mashtalir, J. Carle, V. Presser, J. Lu, L. Hultman, Y. Gogotsi, M.W. Barsoum, ACS Nano 6 (2012) 1322–1331.

[39] C. Xu, L. Wang, Z. Liu, L. Chen, J. Guo, N. Kang, X.-L. Ma, H.-M. Cheng, W. Ren, Nat. Mater. 14 (2015) 1135–1141.

[40] J. Halim, S. Kota, M.R. Lukatskaya, M. Naguib, M.Q. Zhao, E.J. Moon, J. Pitock, J. Nanda, S.J. May, Y. Gogotsi, M.W. Barsoum, Adv. Funct. Mater. 26 (2016) 3118–3127.

[41] M. Naguib, J. Halim, J. Lu, K.M. Cook, L. Hultman, Y. Gogotsi, M.W. Barsoum, J. Am. Chem. Soc. 135 (2013) 15966–15969.

[42] M. Ghidiu, M. Naguib, C. Shi, O. Mashtalir, L.M. Pan, B. Zhang, J. Yang, Y. Gogotsi, S.J.L. Billinge, M.W. Barsoum, Chem. Commun. 50 (2014) 9517–9520.

[43] O. Mashtalir, M.R. Lukatskaya, M.Q. Zhao, M.W. Barsoum, Y. Gogotsi, Adv. Mater. 27 (2015) 3501–3506.

[44] N. Kurra, B. Ahmed, Y. Gogotsi, H.N. Alshareef, Adv. Energy Mater. 6 (2016) 1601372.

[45] M.Q. Zhao, C.E. Ren, Z. Ling, M.R. Lukatskaya, C.F. Zhang, K.L. Van Aken, M.W. Barsoum, Y. Gogotsi, Adv. Mater. 27 (2015) 339–345.

[46] M. Boota, B. Anasori, C. Voigt, M.-Q. Zhao, M.W. Barsoum, Y. Gogotsi, Adv. Mater. 28 (2016) 1517–1522.

[47] Y.-Y. Peng, B. Akuzum, N. Kurra, M.-Q. Zhao, M. Alhabeb, B. Anasori, E.C. Kumbur, H.N. Alshareef, M.-D. Ger, Y. Gogotsi, Energy Environ. Sci. 9 (2016) 2847–2854.

[48] M.R. Lukatskaya, O. Mashtalir, C.E. Ren, Y. Dall'Agnese, P. Rozier, P.L. Taberna, M. Naguib, P. Simon, M.W. Barsoum, Y. Gogotsi, Science 341 (2013) 1502–1505.

[49] M. Ghidiu, M.R. Lukatskaya, M.Q. Zhao, Y. Gogotsi, M.W. Barsoum, Nature 516 (2014) 78–81.

[50] X.Q. Xie, M.Q. Zhao, B. Anasori, K. Maleski, C.E. Ren, J.W. Li, B.W. Byles, E. Pomerantseva, G.X. Wang, Y. Gogotsi, Nano Energy 26 (2016) 513–523.

[51] M. Hu, Z. Li, T. Hu, S. Zhu, C. Zhang, X. Wang, ACS Nano 10 (2016) 11344–11350.

[52] X.H. Wang, Y.C. Zhou, J. Mater. Chem. 12 (2002) 455–460.

[53] J. Li, X. Yuan, C. Lin, Y. Yang, L. Xu, X. Du, J. Xie, J. Lin, J. Sun, Adv. Energy Mater. 7 (2017) 1602725.

[54] J. Zhang, D.-W. Wang, W. Lv, S. Zhang, Q. Liang, D. Zheng, F. Kang, Q.-H. Yang, Energy Environ. Sci. 10 (2017) 370–376.

[55] C. Vaalma, G.A. Giffin, D. Buchholz, S. Passerini, J. Electrochem. Soc. 163 (2016) A1295–A1299.

[56] N. Yabuuchi, K. Kubota, M. Dahbi, S. Komaba, Chem. Rev. 114 (2014) 11636–11682.

[57] Y. Dong, Z.S. Wu, S. Zheng, X. Wang, J. Qin, S. Wang, X. Shi, X. Bao, ACS Nano 11 (2017) 4792–4800.

[58] X. Wu, Z. Wang, M. Yu, L. Xiu, J. Qiu, Adv. Mater. 29 (2017) 1607017.

[59] D. Sun, M. Wang, Z. Li, G. Fan, L.-Z. Fan, A. Zhou, Electrochem. Commun. 47 (2014) 80–83.

[60] X. Zhang, J. Lei, D. Wu, X. Zhao, Y. Jing, Z. Zhou, J. Mater. Chem. A 4 (2016) 4871–4876.

[61] M. Khazaei, M. Arai, T. Sasaki, M. Estili, Y. Sakka, Phys. Chem. Chem. Phys. 16 (2014) 7841–7849.

[62] F. Wang, C. Yang, C. Duan, D. Xiao, Y. Tang, J. Zhu, J. Electrochem. Soc. 162 (2015) B16–B21.

Peichao Lian received his Ph.D. degree from South China University of Technology in 2011. He worked as a visiting scholar in Dalian Institute of Chemical Physics (DICP), Chinese Academy of Sciences (CAS) in 2016. He is now working as an associate professor in Kunming University of Science and Technology. His research interests mainly focus on the synthesis and applications of three-dimensional porous materials.


Yanfeng Dong received his Ph.D. degree in materials science from Dalian University of Technology in 2016. He currently works as a postdoctor at DICP, CAS, advised by Prof. Zhong-Shuai Wu. He has published more than 26 articles in ACS Nano, Adv. Funct. Mater., Nat. Commun., J. Mater. Chem. A etc., with a total citation of more than 540 times. His research focuses on graphene and 2D materials for advanced batteries (e.g., lithium/sodium/potassium ion batteries and Li-S batteries).

Zhong-Shuai Wu received his Ph.D. in materials science from Institute of Metal Research, CAS in 2011, and worked as a postdoctor at Max-Planck Institute for Polymer Research in 2011–2015. Then he joined DICP, CAS, and was appointed as full Professor, and group leader of 2D Materials & Energy Devices. He has published more than 50 research articles in Adv. Mater., Nat. Commun., JACS, ACS Nano etc., with a total citation of more than 11000 times. His research focuses on graphene and 2D materials for supercapacitors, micro-supercapacitors, high-energy batteries (Li-S, Li-, K-, Na-ion), flexible and planar energy-storage devices.


Shuanghao Zheng is now pursuing the Ph.D. degree from Dalian National Laboratory for Clean Energy, DICP, CAS, under the supervision of Prof. Xinhe Bao and Prof. Zhong-Shuai Wu. He obtained B.S. degree in Applied Chemistry from Changsha University of science & Technology in 2014. His research interests focus on graphene & 2D materials, supercapacitors and micro-supercapacitors.
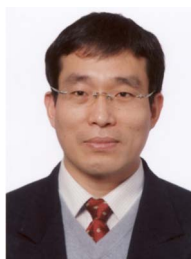
Xiaohui Wang received his Ph.D in 2003 from Institute of Metal Research (IMR), CAS. He then spent almost two years for plasma processing of nanomaterials at the NIMS (Tsukuba, Japan, under Dr. T. Ishigaki). After that, he spent over two years as a postdoctoral fellow at the Tohoku University (Sendai, Japan, under Prof. T. Kyotani). He joined IMR in 2007, and became a full Professor in 2015. His current research interests include LiFePO$_4$ nanomaterials for high-rate lithium-ion batteries, and MAX phases-derived MXenes for energy storage.

Sen Wang received her B.S. degree in 2014 from University of Liaoning. She is currently pursuing her Ph.D. degree under the supervision of Prof. Chenglin Sun and Prof. Zhong-Shuai Wu at DICP, CAS. Her research focuses on the design and fabrication of graphene and 2D materials for micro-supercapacitors and water treatment.
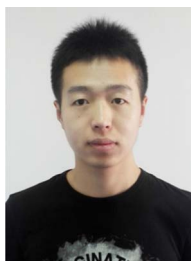
Xiaoyu Shi received his B.S. degree from Nankai University in 2015. He is a Ph.D. candidate at University of Science and Technology of China, co-supervised by Prof. Xinhe Bao and Prof. Zhong-Shuai Wu. His current research focuses on 2D materials for flexible energy storage devices.

Chenglin Sun received his M.S. degree in chemical engineering from DICP, CAS in 1988. After that, he worked in DICP as a research assistant in 1988–1996, and associated professor in 1996–2001. Since 2001, he was promoted a full professor and group leader of Industrial Wastewater Treatment Group. He has published more than 100 research articles and 70 patents. His research focuses on industrial wastewater treatment, development and application of industrial catalyst.

Xinhe Bao received his Ph.D. in Physical Chemistry from Fudan University in 1987. He held an Alexander von Humboldt Research Fellow position in Fritz-Haber Institute between 1989 and 1995, hosted by Prof. Gerhard Ertl. Following that, he joined DICP as a full Professor. He became a member of the CAS in 2009. His research interest is nano and interfacial catalysis, focusing on the fundamental understanding of heterogeneous catalysis, including development of new catalysts and novel catalytic processes related to energy conversion and storage.

Jieqiong Qin is pursuing Ph.D. degree in DICP, CAS, under the supervision of Prof. Zhong-Shuai Wu. She received his M.S. degree in China Research Institute of Daily Chemical Industry in 2016. Her current research focuses on the design and synthesis of graphene and 2D materials and their applications for energy storage devices, such as supercapacitors.